ICME2003-KEY-03

DEVELOPMENT OF MICROCHANNEL HEAT EXCHANGER FOR MAGNETIC REFRIGERATION APPLICATIONS

Muhammad Mustafizur Rahman and Shantanu Sudhir Shevade

Department of Mechanical Engineering
University of South Florida, Tampa, Florida 33620, USA

ABSTRACT

As a first step towards the development of a MEMS magnetocaloric refrigerator an analysis of fluid flow and heat transfer in microchannels was carried out. The study considered microchannels with rectangular and square cross section in Gadolinium and water as the working fluid. Gadolinium is a magnetic material that exhibits high temperature rise during adiabatic magnetization around its transition temperature of 295 K. When subjected to the magnetic field, heat transfer processes during the heat up and cool down phases of a magnetic material were studied. The application of the magnetic field was simulated by using the concept of volumetric heat source distributed uniformly over the entire solid material. Because of the relatively small size of the MEMS device, the magnetic field strength is expected to be uniform throughout the material. The strength of the source was calculated from energy balance during magnetization of the material. Equations governing the conservation of mass, momentum, and energy were solved in the fluid region. In the solid region, heat conduction equation with heat generation was solved. From the simulation results, plots of Nusselt number and heat transfer coefficient were obtained over the length of the channel. A thorough investigation for velocity and temperature distributions was performed by varying channel aspect ratio, Reynolds number, and heat generation rate in the substrate. It was found that the peripheral average heat transfer coefficient and Nusselt number is larger near the entrance and decreases downstream because of the development of the thermal boundary layer. With the increase in Reynolds number, the outlet temperature decreased and the average Nusselt number increased.

Keywords: Microchannel, Transient, Magnetic Refrigeration

INTRODUCTION

Liquid flow and heat transfer in microchannels are critical to the design and process control of various Micro-Electric-Mechanical-Systems (MEMS) and biomedical lab-on-a-chip devices. Experimental and theoretical studies in the literature have shown that a very high rate of heat and mass transfer in microchannels is the key to the extreme efficiencies in the technologies being developed. This study presents a systematic analysis of fluid flow and heat transfer processes during the magnetic heating and cooling of the substrate material. The heating and cooling of magnetic material due to magnetic field occurs due to the magnetocaloric effect. When a strong magnetic field is applied to a magnetic material, the magnetic moments of its atoms become aligned making the system more ordered. The more ordered material has lower entropy and compensates for the loss by heating up. When the magnetic field is removed, the magnetic moments return to their random directions, entropy increases and the material cools. Magnetocaloric effect is found in all transition metals and lanthanide series elements. Gadolinium, Gd5(Si2Ge2) exhibits one of the largest known magnetocaloric effects. Salt pills made up of

Chrome Potassium Alum (CPA) are also useful. CPA has very low ordering temperature that allows cycle to operate with very low temperature. It has a higher melting point so it eliminates concerns over handling and storage. It is proposed to use liquid flow through microchannels fabricated by precision machining of the substrate material for the thermal management of the substrate material during magnetization and demagnetization and use the recovered energy for useful heating or refrigeration. The purpose of this study is to explore the heat transfer coefficient when the fluid is circulated through the substrate via microchannels.

Rujano and Rahman [1] presented numerical simulations of the transient response of the microchannel heat sinks in a silicon wafer analyzing step and pulsed variations of the input heat load. They investigated the dependence of the device transient thermal performance on a variety of parameters such as channel depth, width, length, spacing between channels, Reynolds number, and solid to fluid thermal conductivity ratio. Papautsky et al. [2] described the effects of rectangular microchannel aspect ratio on laminar friction constant. The experimental data obtained for water showed an approximate 20% increase in the friction constant for a

specified driving potential when compared to macro-scale predictions from the classical Navier-Stokes theory. Qu et al. [3] investigated heat transfer characteristics of water flowing through trapezoidal silicon microchannels. A numerical analysis was carried out by solving a conjugate heat transfer problem.

Chen and Wu [4] investigated the microchannel flow in miniature TCDs (thermal conductivity detectors). Effects of channel size and boundary conditions were examined in details. It was found that the change in heat transfer rate in the entrance region depends primarily on the thermal conductivity change in the conduction-dominant region. Pfund et al. [5] determined friction factors for high aspect ratio microchannels. Reynolds numbers were between 60 and 3450. Pressure drops were measured within the channel. Transitions to turbulence were observed with flow visualization. Rahman [6] presented new experimental measurements for pressure drop and heat transfer coefficient in microchannel heat sinks. Tests were performed with devices fabricated using standard Silicon 100 wafers. Channels of different depths (or aspect ratios) were studied. Tests were carried out using water as the working fluid. The fluid flow rate as well as the pressure and temperature of the fluid at the inlet and outlet of the device, and temperature at several locations in the wafer were measured. These measurements were used to calculate local and average Nusselt number and coefficient of friction in the device.

Fedorov and Viskanta [7] developed a three dimensional model to investigate flow and conjugate heat transfer in the microchannel-based heat sink for electronic packaging applications. The analysis provided the complex heat flow pattern established in the channel due to combined convection–conduction effects. Wang et al. [8] studied pressure-driven liquid flow in microchannels. A simple model of flow in microchannels was formulated. The model demonstrated how the capillary force affects the flow and the applicability of boundary layer theory to the flow in a microchannel. Lee et al. [9] fabricated a series of microchannels using standard micromachining techniques. The mass flow rate and pressure measurements indicated the existence of flow separation in the microchannels. Quadir et al. [10] applied a finite element method to evaluate the performance of microchannel heat exchangers. The finite element method was proved satisfactory to predict the surface temperature, the fluid temperature and thus the total thermal resistance of the microchannel heat sink. Bendib and Olivier [11] studied microchannels, fabricated by micromachining technology. Results from simulation as well as analytical study were presented.

Zhao and Liao [12] presented a mathematical model predicting combined electro-osmotic and pressure-driven flow behavior in a straight microchannel. The governing equations were solved numerically using a finite difference method. Yang et al. [13] studied electroosmotic flow in a slit microchannel. The characteristics of the electroosmotic flow were discussed under influences of electric double layer and geometric size of the microchannel.

Jiang et al. [14] fabricated integrated microsystem consisting of microchannels. The transient temperature behavior of the device was experimentally studied for a variety of power dissipation levels. Water was used as the working fluid. Both heating-up and cooling-down time constants were determined for a pulsed current input. It was found that, contrary to expectations, the heating-up time constant was larger than the cooling-down time constant.

DeGregoria et al. [15] tested an experimental magnetocaloric refrigerator designed to operate within temperature range of about 4 to 80 K. Helium gas was used as a heat transfer fluid. A single magnet was used to charge and discharge two in-line beds of magnetocaloric material. Zimm et al. [16] investigated magnetic refrigeration for near room temperature cooling. Water was used as the heat transfer fluid. A porous bed of magnetocaloric material was used in the experiment. It was found that using a 5T magnetic field, a refrigerator reliably produces cooling powers exceeding 500W at coefficient of performance 6 or more. Pecharsky and Gschneidner [17] discussed new materials with respect to their magnetocaloric properties. Recent progress in magnetocaloric refrigerator design was reviewed.

The present investigation has the following objectives:
1) To develop simulation model for fluid flow and heat transfer in microchannels.
2) To study microchannels with rectangular and square cross section with heat generation in the substrate due to imposed magnetic field.
3) To calculate velocity and temperature distributions for various channel aspect ratios, Reynolds numbers, and heat generation rates in the substrate.
4) To explore the variation of steady and transient heat transfer coefficient and Nusselt number.

NOMENCLATURE

B Substrate width, m
B_c Channel width, m
C_p Constant pressure specific heat, J/kgK
D_h Hydraulic diameter, m
Fo   Fourier number, $\alpha_f t/D_h^2$, Dimensionless
g_0 Heat generation within the solid, W/m^3
h Heat transfer coefficient, $q_{int}/(T_{int}-T_b)$, W/m^{2}K
H Height of the substrate, m
Hc   Channel height, m
k Thermal conductivity, W/mK; or Turbulent kinetic energy, m^2/s^2
L Channel length, m
Nu   Nusselt number, hD_h/k_f, Dimensionless
p Pressure, N/m^2
Pr$_t$ Turbulent Prandtl number, Dimensionless
q Heat flux, W/m^2
Re   Reynolds number, $w_{in}D_h/v_f$, Dimensionless
t Time, s
T Temperature, ^{0}C
u Velocity in x-direction, m/s
v Velocity in y-direction, m/s
w Velocity in z-direction, m/s
x Distance in x-direction, m
y Distance in y-direction, m

z Distance in z-direction, m
Greek symbols
α Thermal diffusivity, m^2/s
ε Dissipation rate of turbulent kinetic energy, m^2/s^3
ν Kinematic viscosity, m^2/s
ν_t Turbulent viscosity, m^2/s
ρ Density, kg/m^3
Subscripts
b Bulk
f Fluid
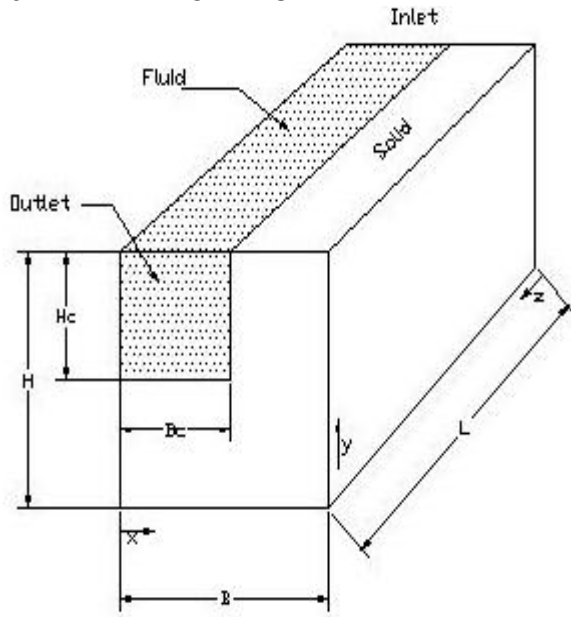in Inlet
int Interface
max Maximum
s Solid

3.0 MATHEMATICAL MODEL

Figure 1: Schematic of microchannel heat exchanger

The physical configuration of the system used is schematically shown in figure 1. Because of the symmetry of adjacent channels in both horizontal and vertical directions, the analysis can be performed by considering a cross section of the heat exchanger containing half of distance between channels in horizontal as well as vertical directions. Neglecting the effects of inlet and outlet plenums, it was assumed that the fluid enters the channel with a uniform velocity and temperature.

The equations for the conservation of mass, momentum, and energy in Cartesian coordinate system are [18],

$$\frac{\partial u}{\partial x} + \frac{\partial v}{\partial y} + \frac{\partial w}{\partial z} = 0 \tag{1}$$

$$u\frac{\partial u}{\partial x} + v\frac{\partial u}{\partial y} + w\frac{\partial u}{\partial z} = -\frac{1}{\rho}\frac{\partial p}{\partial x} + \frac{\partial}{\partial x}\left[(v+v_t)\frac{\partial u}{\partial x}\right]$$
$$+ \frac{\partial}{\partial y}\left[(v+v_t)\frac{\partial u}{\partial y}\right] + \frac{\partial}{\partial z}\left[(v+v_t)\frac{\partial u}{\partial z}\right] \tag{2}$$

$$u\frac{\partial v}{\partial x} + v\frac{\partial v}{\partial y} + w\frac{\partial v}{\partial z} = -\frac{1}{\rho}\frac{\partial p}{\partial y} + \frac{\partial}{\partial x}\left[(v+v_t)\frac{\partial v}{\partial x}\right]$$
$$+ \frac{\partial}{\partial y}\left[(v+v_t)\frac{\partial v}{\partial y}\right] + \frac{\partial}{\partial z}\left[(v+v_t)\frac{\partial v}{\partial z}\right] \tag{3}$$

$$u\frac{\partial w}{\partial x} + v\frac{\partial w}{\partial y} + w\frac{\partial w}{\partial z} = -\frac{1}{\rho}\frac{\partial p}{\partial z} + \frac{\partial}{\partial x}\left[(v+v_t)\frac{\partial w}{\partial x}\right]$$
$$\frac{\partial}{\partial y}\left[(v+v_t)\frac{\partial w}{\partial y}\right] + \frac{\partial}{\partial z}\left[(v+v_t)\frac{\partial w}{\partial z}\right] \tag{4}$$

The k-ε model was used for simulation of turbulence. In this model, equations governing the conservation of turbulent kinetic energy and its rate of dissipation were solved. These equations can be expressed as,

$$u\frac{\partial k}{\partial x} + v\frac{\partial k}{\partial y} + w\frac{\partial k}{\partial z}$$
$$= \frac{\partial}{\partial x}\left[\left(v+\frac{v_t}{\sigma_k}\right)\frac{\partial k}{\partial x}\right] + \frac{\partial}{\partial y}\left[\left(v+\frac{v_t}{\sigma_k}\right)\frac{\partial k}{\partial y}\right] +$$
$$\frac{\partial}{\partial z}\left[\left(v+\frac{v_t}{\sigma_k}\right)\frac{\partial k}{\partial z}\right] + v_t\left[\left(\frac{\partial u}{\partial y}\right)^2 + \left(\frac{\partial u}{\partial z}\right)^2 + \left(\frac{\partial v}{\partial x}\right)^2\right.$$
$$\left. + \left(\frac{\partial v}{\partial z}\right)^2 + \left(\frac{\partial w}{\partial x}\right)^2 + \left(\frac{\partial w}{\partial y}\right)^2\right] - \varepsilon \tag{5}$$

$$u\frac{\partial \varepsilon}{\partial x} + v\frac{\partial \varepsilon}{\partial y} + w\frac{\partial \varepsilon}{\partial z}$$
$$= \frac{\partial}{\partial x}\left[\left(v+\frac{v_t}{\sigma_\varepsilon}\right)\frac{\partial \varepsilon}{\partial x}\right] + \frac{\partial}{\partial y}\left[\left(v+\frac{v_t}{\sigma_\varepsilon}\right)\frac{\partial \varepsilon}{\partial y}\right]$$
$$+ \frac{\partial}{\partial z}\left[\left(v+\frac{v_t}{\sigma_\varepsilon}\right)\frac{\partial \varepsilon}{\partial z}\right] + C_1\frac{\varepsilon}{k}v_t\left[\left(\frac{\partial u}{\partial y}\right)^2 + \left(\frac{\partial u}{\partial z}\right)^2\right.$$
$$\left. + \left(\frac{\partial v}{\partial x}\right)^2 + \left(\frac{\partial v}{\partial z}\right)^2 + \left(\frac{\partial w}{\partial x}\right)^2 + \left(\frac{\partial w}{\partial y}\right)^2\right] - C_2\frac{\varepsilon^2}{k} \tag{6}$$

© ICME2003

$$v_t = C_\mu k^2 / \varepsilon \qquad (7)$$

The empirical constants appearing in equations (5)-(7) are given by the following values, $C_\mu=0.09$, $C_1=1.44$, $C_2=1.92$, $\sigma_k=1.0$, $\sigma_\varepsilon=1.3$. The energy equation in the fluid region is,

$$\frac{\partial T_f}{\partial t} + u\frac{\partial T_f}{\partial x} + v\frac{\partial T_f}{\partial y} + w\frac{\partial T_f}{\partial z}$$

$$= \left(\alpha_f + \frac{v_t}{Pr_t}\right)\left[\frac{\partial^2 T_f}{\partial x^2} + \frac{\partial^2 T_f}{\partial y^2} + \frac{\partial^2 T_f}{\partial z^2}\right]$$

$$(8)$$

The equation for heat conduction in the solid region is,

$$\frac{\partial^2 T_s}{\partial x^2} + \frac{\partial^2 T_s}{\partial y^2} + \frac{\partial^2 T_s}{\partial z^2} + \frac{g_0}{k_s} = \frac{1}{\alpha_s}\frac{\partial T_s}{\partial t} \qquad (9)$$

To complete the physical model, equations (1) to (9) are subjected to the following initial and boundary conditions:

At t=0, $T_s=T_{in}$, $T_f=T_{in}$ (for transient simulations) (10)

At z=0, 0<x<Bc, (H-Hc)<y<H, u=0, v=0, w=w$_{in}$, T= T$_{in}$
$$(11)$$

At z=0, 0<x<Bc and 0<y<(H-Hc), Bc<x<B and 0<y<H,
$$\frac{\partial T_s}{\partial z} = 0 \qquad (12)$$

At z=L, 0<x<Bc, (H-Hc)<y<H, p=0 (13)

At z=L, 0<x<Bc and 0<y<(H-Hc), Bc<x<B and 0<y<H,

$$\frac{\partial T_s}{\partial z} = 0 \qquad (14)$$
At x=0, (H-Hc)<y<H, 0<z<L,

$$u=0, \frac{\partial v}{\partial x} = 0, \frac{\partial w}{\partial x} = 0, \frac{\partial T_f}{\partial x} = 0$$
$$(15)$$

At x=0, 0<y<(H-Hc), 0<z<L, $\frac{\partial T_s}{\partial x} = 0$ (16)

At x=B, 0<y<H, 0<z<L, $\frac{\partial T_s}{\partial x} = 0$ (17)

At y=0, 0<x<B, 0<z<L, $\frac{\partial T_s}{\partial y} = 0$ (18)

At y=H, 0<x<Bc, 0<z<L,

$$v=0, \frac{\partial u}{\partial x} = 0, \frac{\partial w}{\partial y} = 0, \frac{\partial T_f}{\partial y} = 0 \qquad (19)$$

At y=H, Bc<x<B, 0<z<L, $\frac{\partial T_s}{\partial y} = 0$ (20)

At y= (H-Hc), 0<x<Bc, 0<z<L,

$$T_{f=T_s}, \ k_f\frac{\partial T_f}{\partial y} = k_s\frac{\partial T_s}{\partial y} \qquad (21)$$
At x= Bc, (H-Hc)<y<H, 0<z<L,

$$T_{f=T_s}, \ k_f\frac{\partial T_f}{\partial x} = k_s\frac{\partial T_s}{\partial x} \qquad (22)$$

NUMERICAL SIMULATION

The investigation for velocity and temperature distribution was performed by varying channel aspect ratio, Reynolds number, and heat generation rate in the channel. The results computed were for Gadolinium substrate and water as the working fluid.

For all the configurations studied the length of the microchannel (L) was kept constant at 25 mm. The channel was tested for different aspect ratios. For most runs, heat generation rate within the solid (g_0) was taken as 6.4E8 W/m^3 during the heating phase. This generation rate corresponded to an adiabatic temperature rise of 11.8K in gadolinium when subjected to a magnetic field of 5T. During cooling phase heat generation rate was taken to be -6.4E8 W/m^3. The governing equations along with the boundary conditions were solved by using the Galerkin finite element method. Four-node quadrilateral elements were used. In each element, the velocity, pressure, and temperature fields were approximated which led to a set of equations that defined the continuum. An iterative procedure was used to arrive at the solution for the velocity and temperature fields. The solution was considered converged when the field values did not change from one iteration to the next. A systematic grid independence study was carried out by varying the number of elements in the x, y, and z directions. It was found that the results obtained by using 16x16x96 and those with 64x64x384 elements provided interface temperature distributions within 1%. Therefore, 16x16x96 elements in x, y, and z directions were used in all numerical simulations presented here.

RESULTS FOR STEADY STATE HEAT TRANSFER

The local heat transfer coefficient and local Nusselt number were calculated at locations z/L=0.25 and z/L=0.75. Figure 2 shows the variation of Nusselt number over dimensionless coordinate (x/B) of the channel for different aspect ratios for Re=3000 and g_0=6.4E8 W/m^3. It is seen that as one moves along the

4

x-axis i.e. from the symmetric boundary to the solid, the value of Nusselt number decreases. The velocity of fluid at symmetric boundary is higher than the velocity of fluid near channel walls. Therefore the Nusselt number goes on decreasing along the x-axis of the channel. The decrease in monotonic and more as one approaches the
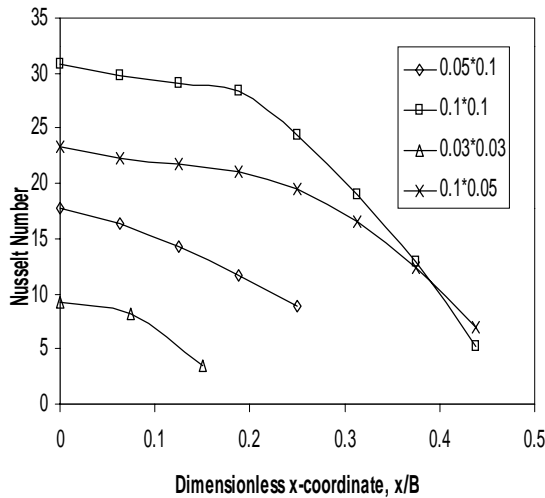
number goes on increasing. It reaches the peak at the symmetric boundary. High velocity of fluid at the symmetric boundary explains high Nusselt number at the boundary. The values of Nusselt number are higher in channels with higher hydraulic diameter.

Figure 2: Variation of Nusselt number over dimensionless coordinate (x/B) for different aspect ratios (Bc*Hc) of the channel. (z/L=0.25, Re=3000)

corner. Comparing the two square channels it is seen that the Nusselt number values of bigger channel (0.1 cm * 0.1 cm) are higher than the Nusselt number values of smaller channel (0.03 cm * 0.03 cm). Even though the heat transfer coefficients in these two cases were on the same order of magnitude, a smaller hydraulic diameter for the smaller channel has resulted in lower Nusselt number.
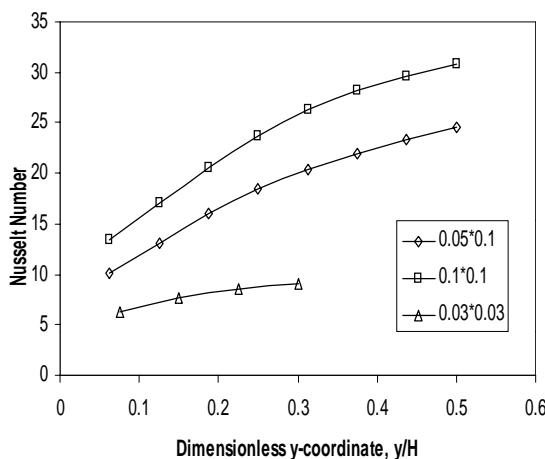
Figure 3: Variation of Nusselt number over dimensionless coordinate (y/H) for different aspect ratios (Bc*Hc) of the channel. (z/L=0.25, Re=3000)

Figure 3 shows the Nusselt number variation over dimensionless coordinate (y/H) of the channel for different aspect ratios for Re=3000 and g_0= 6.4E8 W/m^3. As one moves along the y-axis, the value of Nusselt

Figure 4: Variation of Nusselt number over dimensionless coordinate (x/B) for different aspect ratios (Bc*Hc) of the channel. (z/L=0.75, Re=3000)

Figure 4 shows the variation of local Nusselt number over dimensionless coordinate (x/B) of the channel for different aspect ratios at z/L=0.75 for Re=3000 and g_0= 6.4E8 W/m^3. As compared to the values at z/L=0.25 it is seen that the Nusselt number values are less at z/L=0.75. The trend remains the same. A lower value of Nusselt number downstream in the flow direction is expected because the fluid becomes warmer and loses its potential to carry away heat from the wall.
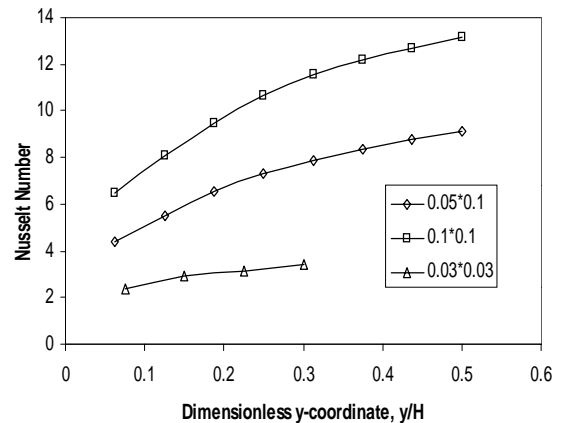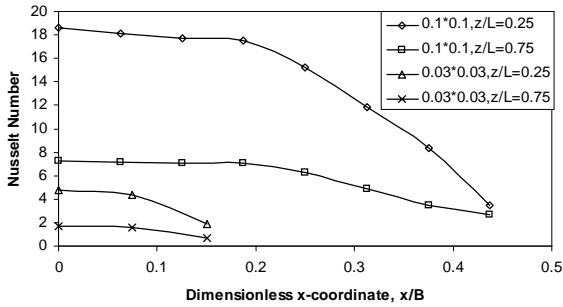

Figure 5: Variation of Nusselt number over dimensionless coordinate (y/H) for different aspect ratios(Bc*Hc) of the channel. (z/L=0.75, Re=3000)

Figure 5 shows variation of Nusselt number over dimensionless coordinate (y/H) for different channel aspect ratios for Re=3000 and g_0= 6.4E8 W/m^3. Analogous to figure 3, as one moves along the y-axis, the value of Nusselt number goes on increasing and reaches the peak at the symmetric boundary. The magnitude of Nusselt number at z/L=0.75 is however significantly lower than that at z/L=0.25 due to higher thickness of

thermal boundary layer as the flow and heat transfer approaches the fully developed condition.

Figure 6 shows the variation of local Nusselt number over dimensionless coordinate (x/B) at z/L=0.25 and z/L=0.75 for Reynolds number of 1600. As compared to the same channel with fluid flowing at higher Reynolds number, the corresponding values of Nusselt number are lower. On the other hand, the outlet temperature of the fluid is increased as the fluid remains in contact with the solid for longer time. The difference in the values of Nusselt number at the two locations become smaller at lower Reynolds number because the flow approaches the fully developed condition at a smaller distance downstream from the entrance.

Figure 6: Variation of Nusselt number over dimensionless coordinate (x/B) for different aspect ratios (Bc*Hc) of the channel. (Re=1600)
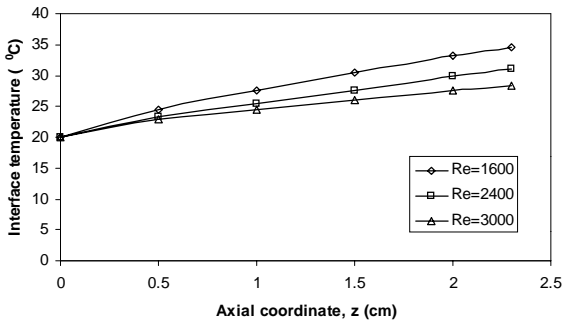
Figure 7: Variation of peripheral average interface temperature along the channel axial length for different Reynolds number
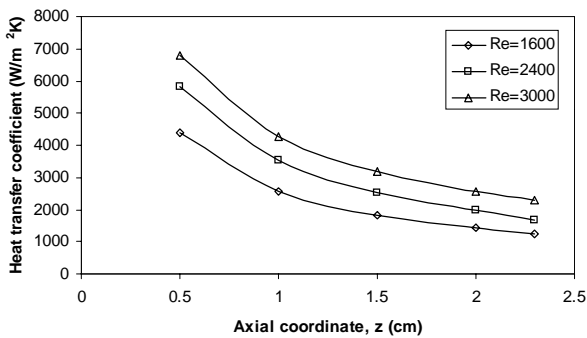
Figure 8: Variation of heat transfer coefficient along the channel length for different Reynolds number

Figure 7 shows variation of interface temperature for different Reynolds number for channel with 0.1*0.1cm

aspect ratio. The solid-fluid interface temperature increases as the fluid moves downstream due to the development of thermal boundary layer starting with the entrance section as the leading edge. It can be seen that as the Reynolds number increases, the interface temperature decreases. For lower Reynolds number fluid remains in contact with the solid for longer time. Thus, higher interface temperature values are obtained.

Figure 8 shows the variation of peripheral average heat transfer coefficient for different Reynolds number for channel with 0.1*0.1 cm aspect ratio. Heat transfer coefficient is seen to be increasing with increase in Reynolds number. Heat transfer coefficient decreases along the channel length. Fluid gets heated as it passes through the channel. The temperature difference between fluid and solid decreases as one moves along the length of the channel. Thermal boundary layer grows until fully developed flow is produced. Therefore the heat transfer coefficient is higher at the entrance and decreases downstream. The variation is larger at the entrance because of the rapid development of thermal boundary layer near the leading edge.

Figure 9 shows the variation of peripheral average Nusselt number with dimensionless axial coordinate for different Reynolds number for 0.1*0.1cm aspect ratio. The trends are analogous to that seen for the variation of heat transfer coefficient presented in figure 8.
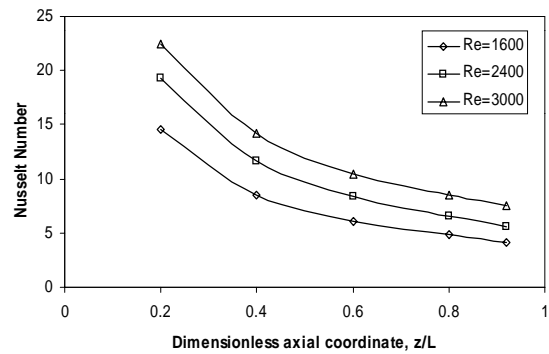

Figure 9: Variation of Nusselt number along the channel length for different Reynolds number

Table 1: Physical configuration of microchannels

Channel aspect ratio (Bc*Hc)	D_h	Solid volume / Total volume	Channel surface area / Solid volume
(cm)	(cm)		(cm^{-1})
0.1*0.1	0.2	0.75	6.6667
0.05*0.1	0.1334	0.875	4.2857
0.1*0.05	0.1334	0.75	10
0.03*0.03	0.06	0.955	3.1413

Table 1 presents the hydraulic diameter, ratio of solid to total volume, and ratio of channel surface area to solid volume for each of these microchannel heat exchangers. For a given Reynolds number, the channel with smaller

6

hydraulic diameter results in larger fluid velocity and therefore a larger rate of convective heat transfer at the solid-fluid interface. A larger solid to total volume ratio indicates a larger rate of heat generation due to magnetic field whereas smaller amount of fluid available to carry away that heat if the total volume of the heat exchanger is
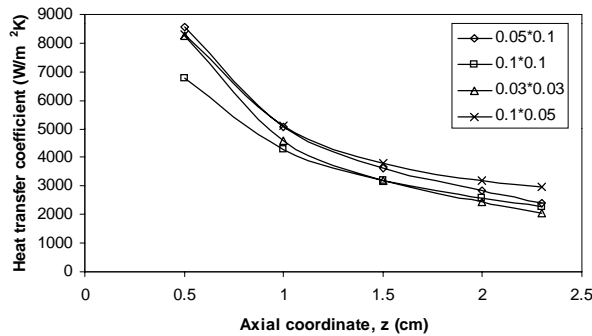

Figure 10: Variation of Heat transfer coefficient along the channel length for different aspect ratios (Bc*Hc)

maintained constant. A larger channel surface area to solid volume ratio indicates that more surface area is available to dissipate a given rate of heat generation. A complex interaction of these three parameters control the conjugate heat transfer process encountered in this kind of microchannel heat exchanger.

Figure 10 shows the variation of heat transfer coefficient along the length of the channel for different aspect ratios for Re=3000 and g_0= 6.4E8 W/m^3. The values of heat transfer coefficient are higher in rectangular channel as compared to those of square channel. In square channels, heat transfer coefficient values of smaller channel are greater than those of a bigger channel because of larger fluid velocity that enhances convection at the solid-fluid interface.
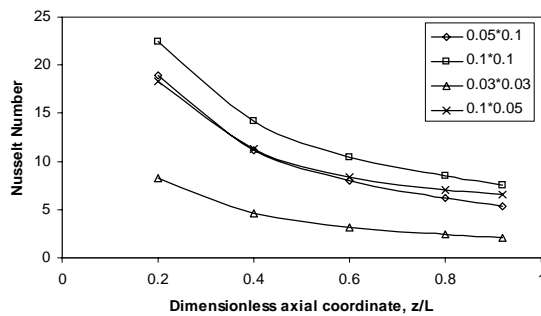
Figure 11: Variation of Nusselt number along the channel length for different aspect ratios (Bc*Hc)

Figure 11 shows variation of Nusselt number for different channel aspect ratios for Re=3000 and g_0= 6.4E8 W/m^3. Nusselt number shows the same trend as that of heat transfer coefficient. Nusselt number curves are spread out as compared to heat transfer coefficient curves as the hydraulic diameter is different for different channels.

Figure 12 shows variation of Nusselt number for different heat generation rates for Re=3000 and aspect ratio of 0.1*0.1 cm. Nusselt number at a particular cross section in the channel remains almost the same for different heat generation rates.

Figure 13 shows variation of maximum temperature in the solid for different aspect ratios of the channel for g_0= 6.4E8 W/m^3. The data is collected for different Reynolds number. Temperature is maximum for the smallest square channel. Maximum temperature in the
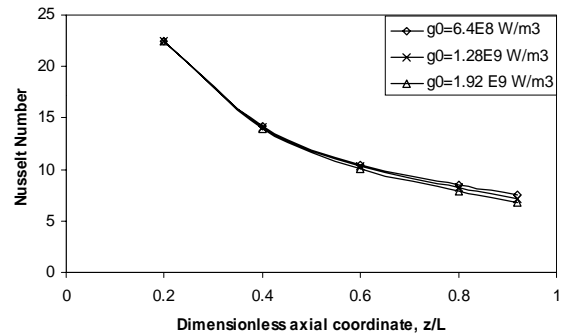

Figure 12: Variation of Nusselt number along the channel length for different heat generation rates

channel drops down as the hydraulic diameter increases. For the same channel, maximum temperature decreases as the Reynolds number increases. The values of maximum temperature are higher for the channel with larger amount of solid. As the amount of the solid surrounding the microchannel decreases, maximum temperature in the microchannel decreases. The maximum temperature in the microchannel is found in solid region at the outlet edge of the channel.
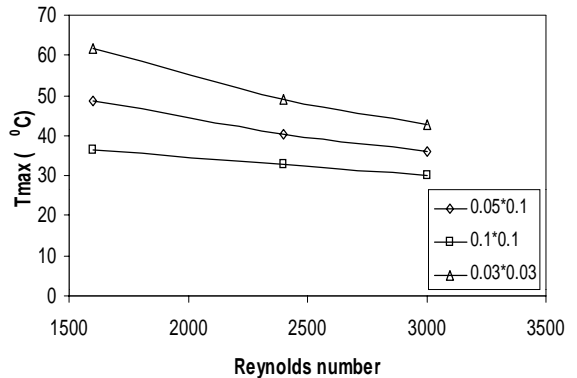

Figure 13: Variation of maximum temperature for different aspect ratios (Bc*Hc)

Figure 14 shows variation of pressure drop in the channel for different channel aspect ratios for g_0= 6.4E8 W/m^3. The data is collected for different Reynolds number. It can be seen that the values of pressure difference between inlet and outlet of the channel are highest for smallest square channel. This is expected because the flow encounters a larger frictional resistance from the walls. The pressure difference increases as the Reynolds number increases.

Figure 15 shows variation of average heat transfer coefficient for the channel for different channel aspect ratios for g_0= 6.4E8 W/m^3. The data is collected at different Reynolds number. Heat transfer coefficient is more in the rectangular channel compared to the two

7

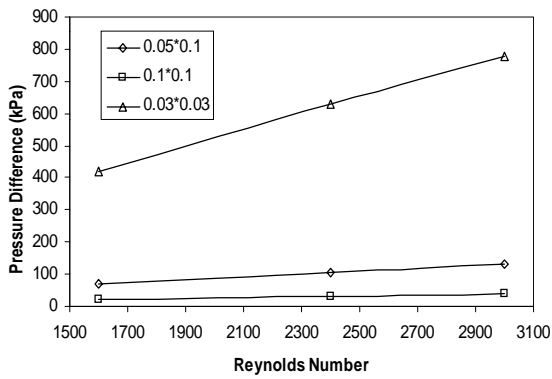square channels. For the same channel heat transfer coefficient increases as Reynolds number increases.

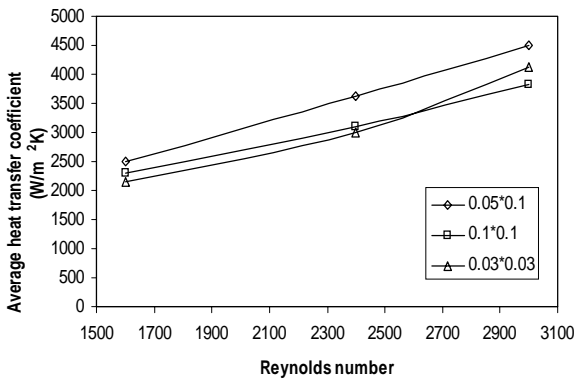Figure 14: Variation of pressure difference for different aspect ratios (Bc*Hc)

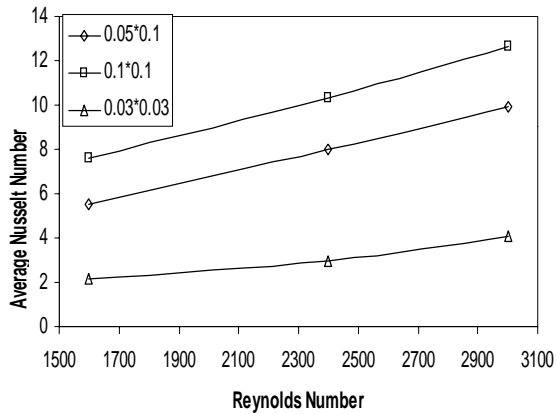Figure 15: Variation of average heat transfer coefficient for different aspect ratios (Bc*Hc)

Figure 16: Variation of average Nusselt number for different aspect ratios (Bc*Hc)

Figure 16 shows variation of average Nusselt number for different channel aspect ratios for $g_0 = 6.4E8$ W/m^3. The data is collected at different Reynolds number. Nusselt number shows the same trend as that of heat transfer coefficient. Nusselt number curves are spread out as compared to heat transfer coefficient curves as the hydraulic diameter is different for different channels.

RESULTS FOR TRANSIENT START-UP OF HEATING

The transient heating process, when the heat exchanger is exposed to the magnetic field was studied. The volumetric heat source was turned on at t=0, and the variation of temperature were studied as the time progressed until the steady state condition was arrived. The results computed were for Gadolinium substrate and water as the working fluid. The parameters were calculated at different sections along the length of the channel for different time intervals.
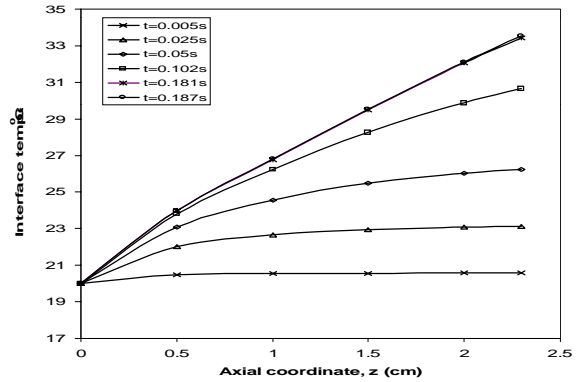

Figure 17: Variation of interface temperature along the length of the channel for different time intervals (Re=3000, Bc=0.05 cm, Hc=0.1 cm, $g_0 = 6.4E8$ W/m^3)

Figure 17 shows the variation of peripheral average interface temperature at different locations along the length of the channel at different time intervals. Reynolds number is 3000. The heat generation rate within the substrate is 6.4E8 W/m^3. The solid-fluid interface temperature increases as the fluid moves downstream due to the development of thermal boundary layer starting with the entrance section as the leading edge. The highest value of interface temperature is seen near the outlet of the channel. Interface temperature rises as the time increases. It can be seen from the graph that, at 0.187s the interface temperature reaches the steady state condition. There is no further change in interface temperature even though the heat generation continues for a longer period of time.
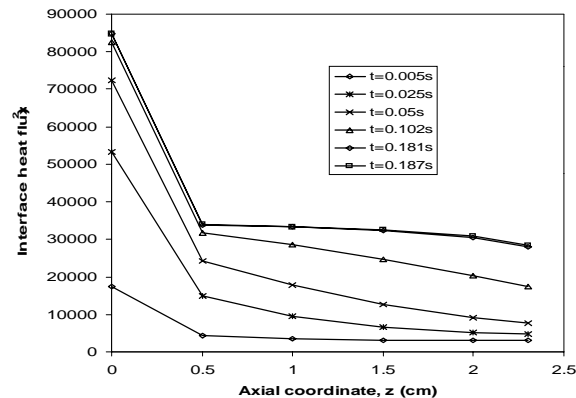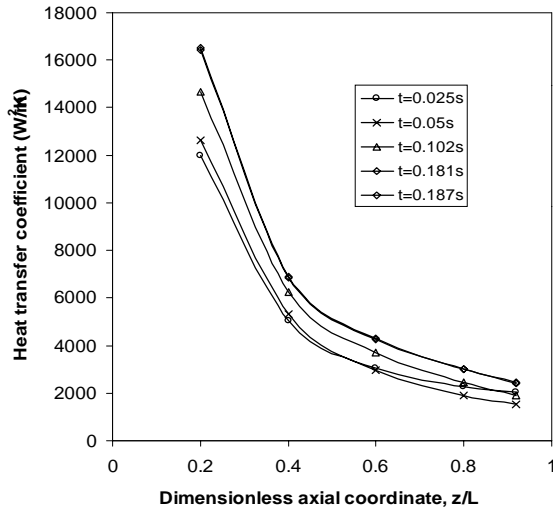

Figure 18: Variation of interface heat flux along the length of the channel for different time intervals (Re=3000, Bc=0.05 cm, Hc=0.1 cm, $g_0 = 6.4E8$ W/m^3)

Figure 18 shows the variation of interface heat flux at different locations along the length of the channel for different time intervals. Reynolds number is 3000. Interface heat flux decreases as the fluid moves along the length of the channel. At the entrance, the values of interface heat flux are higher because of the larger temperature difference between solid and fluid. As the time increases, interface heat flux goes on increasing. It reaches the steady state condition, after which there is no further increase in interface heat flux.

Figure 19: Variation of heat transfer coefficient along the length of the channel for different time intervals (Re=3000, Bc=0.05 cm, Hc=0.1 cm, g_0= 6.4E8 W/m^3)
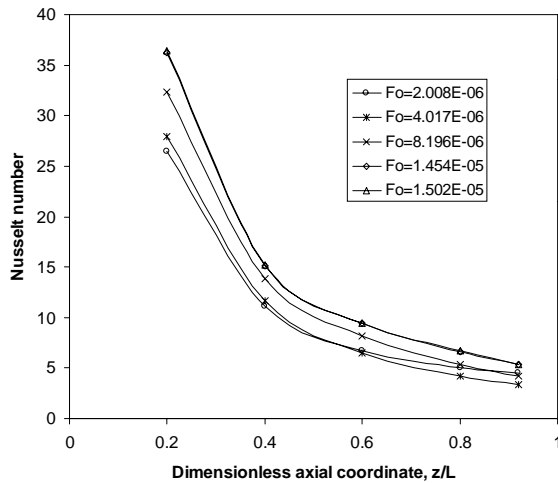

Figure 20: Variation of Nusselt number along the length of the channel for different time intervals (Re=3000, Bc=0.05 cm, Hc=0.1 cm, g_0= 6.4E8 W/m^3)

Figure 19 shows the variation of heat transfer coefficient at different sections along the length of a channel for different time intervals. Reynolds number of the fluid is 3000 and channel dimensions are 0.05*0.1cm. Heat transfer coefficient decreases along the channel length. Fluid gets heated as it passes through the channel. The temperature difference between fluid and solid decreases as one moves along the length of the channel. Thermal boundary layer grows until fully developed

flow is produced. Therefore, the heat transfer coefficient is higher at the entrance and decreases downstream. The variation is larger at the entrance because of the rapid development of thermal boundary layer near the leading edge. Heat transfer coefficient values increase as the time is increased until the steady state condition is arrived.

Figure 20 shows the variation of Nusselt number at different locations along the length of the channel for different Fourier numbers. Reynolds number is 3000. The trends are analogous to that seen for the variation of heat transfer coefficient presented in figure 19. For this channel, the steady state condition is reached at Fo= 1.50 E-5.
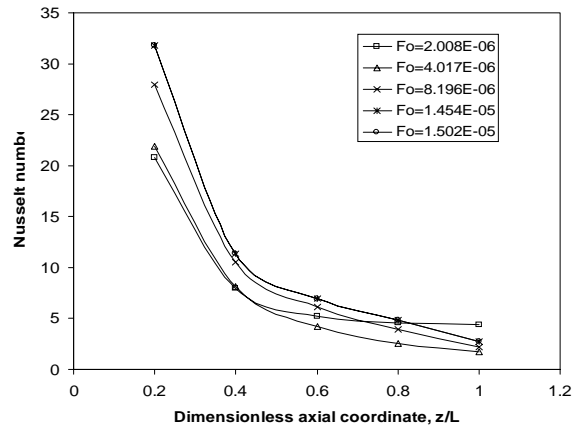

Figure 21: Variation of Nusselt number along the length of the channel for different time intervals (Re=2000, Bc=0.05 cm, Hc=0.1 cm, g_0= 6.4E8 W/m^3)

Figure 21 shows the variation of Nusselt number at different locations along the length of the channel for different Fourier numbers. Reynolds number of the fluid is 2000. Nusselt number is seen to be decreasing along the length of the channel. It shows higher values at the entrance because of the higher temperature difference between solid and fluid near the inlet of the channel. As the Reynolds number decreases fluid remains in contact with solid for a longer time. This lowers down the heat transfer coefficient. Therefore, Nusselt number values are seen to be lower compared to that in figure 20.
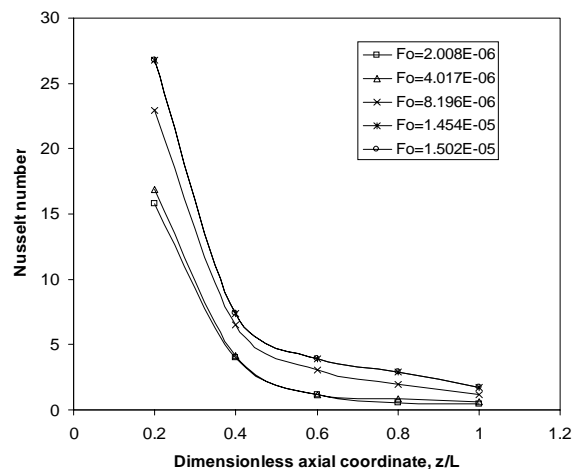

Figure 22: Variation of Nusselt number along the length of the channel for different time intervals (Re=1000, Bc=0.05 cm, Hc=0.1 cm, g_0= 6.4E8 W/m^3)

Figure 22 shows the variation of Nusselt number at different locations along the length of the channel at different Fourier numbers for Reynolds number of 1000. It may be noted that, analogous to figures 20 and 21, the Nusselt number increases with time all along the channel and reaches the steady state distribution. The magnitude of Nusselt number during this transient process however, is very significantly affected by the magnitude of Reynolds number.
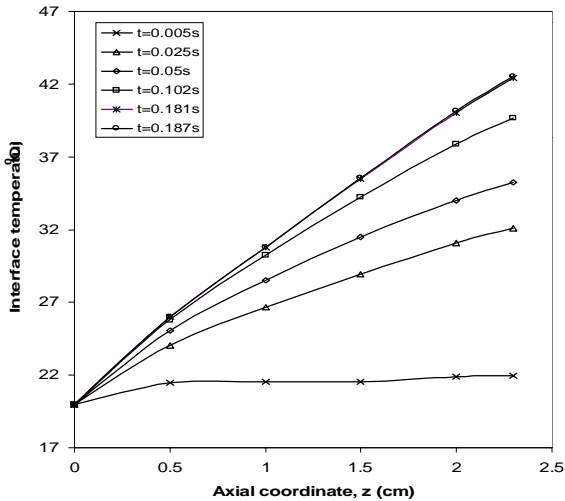
Figure 23: Variation of interface temperature along the length of the channel for different time intervals (Re=3000, Bc=0.05 cm, Hc=0.1 cm, g_0= 12.8E8 W/m^3)
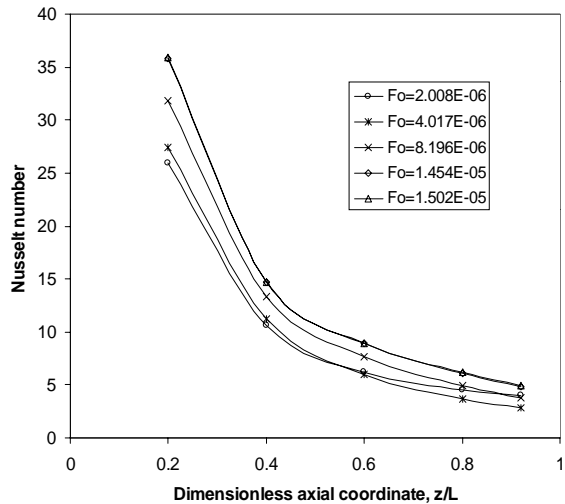
Figure 24: Variation of Nusselt number along the length of the channel for different time intervals (Re=3000, Bc=0.05 cm, Hc=0.1 cm, g_0= 12.8E8 W/m^3)

Figure 23 shows the variation of interface temperature at different locations along the length of the channel for different time intervals. The heat generation rate within the substrate is 12.8E8 W/m^3. Reynolds number is 3000 and channel dimensions are 0.05*0.1 cm. As the heat generation rate is doubled, more heat is passed to the flowing fluid. As compared to figure 17, the interface temperature increased quite significantly. Figure 24 shows the variation of Nusselt number along the length of the channel for different Fourier numbers.

Nusselt number increases with time and reaches the steady state condition. However, Nusselt number values obtained in this case are similar to those in figure 20. Thus, there is no significant increase in the magnitude of Nusselt number as the heat generation rate is doubled.
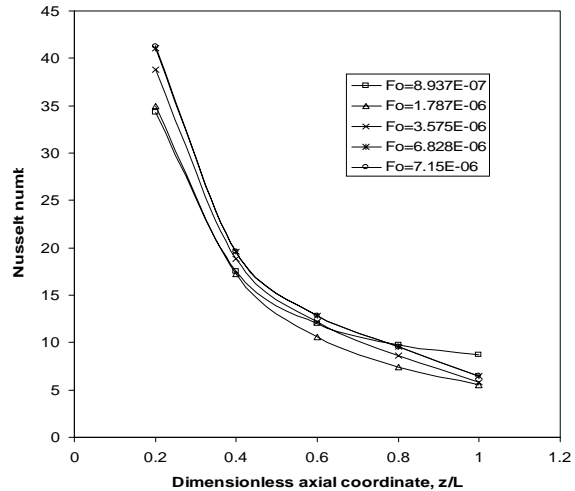
Figure 25: Variation of Nusselt number along the length of the channel for different time intervals (Re=3000, Bc=0.1 cm, Hc=0.1 cm, g_0= 6.4E8 W/m^3)

Figure 25 shows the variation of Nusselt number at different locations along the length of the channel for different time intervals. Reynolds number is 3000 and channel dimensions are 0.1*0.1 cm. As compared to a rectangular channel with dimensions of 0.05*0.1 cm, more amount of fluid is passing through this square channel. Therefore, the values of interface temperature are lower than that of the rectangular channel. This results in somewhat higher values of heat transfer coefficient and consequently higher Nusselt number.

RESULTS FOR PERIODIC HEATING AND COOLING

The transient heating and cooling process, when the heat exchanger is exposed to the fluctuating magnetic field was studied. The volumetric heat source was turned on and off for certain period of time, and the variations of temperature and Nusselt number were studied. The results computed were for Gadolinium substrate and water as the working fluid. The parameters were calculated at different sections along the length of the channel for different time intervals.
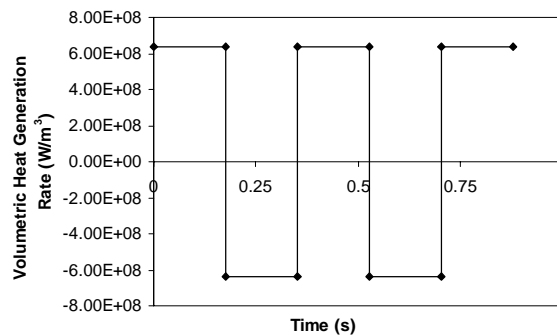
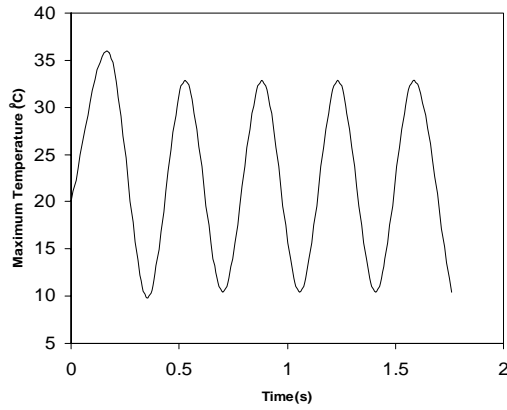Figure 26: Variation of volumetric heat generation rate with time.

10

Figure 27: Variation of maximum temperature in the substrate (Re=1600, Bc=0.05 cm, Hc=0.1 cm, g_0= 6.4E8 W/m^3)

Figure 26 shows the variation of volumetric heat generation rate with time. When a magnetic field of 5T is applied to the microchannel heat exchanger, 6.4E8 W/m^3 of heat is generated and the magnetic material heats up. When the magnetic field is removed, the material cools down. The negative heat generation rate of -6.4E8 W/m^3 shows the condition when the magnetic field of 5T is removed.

Figure 27 shows the variation of maximum temperature in the substrate with time for heating and cooling cycles. Reynolds number is 1600. The maximum temperature in the microchannel is found in the solid region at the outlet edge of the channel. A sinusoidal behavior of the temperature is seen for the heating and cooling cycles. After a small time period the maximum temperature maintains fluctuations between 33^{0}C and 10^{0}C.

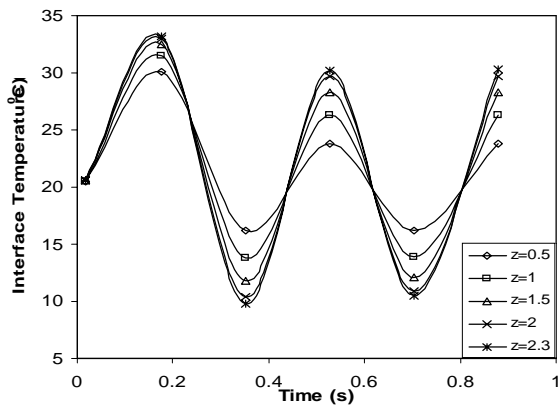Figure 28: Variation of interface temperature with time at different sections in the rectangular channel (Re=1600, Bc=0.05 cm, Hc=0.1 cm, g_0= 6.4E8 W/m^3)

Figure 28 shows the variation of peripheral average interface temperature with time at different locations along the length of the channel for Re=1600. During the heating phase as the fluid passes along the length of the channel it gains heat. The solid-fluid interface temperature increases as the fluid moves downstream due to the development of thermal boundary layer starting with the entrance section as the leading edge. During the cooling phase the solid-fluid interface

temperature decreases. Fluid cools down as the heat is taken out from the fluid. The highest values of interface temperature are seen near the outlet of the channel.
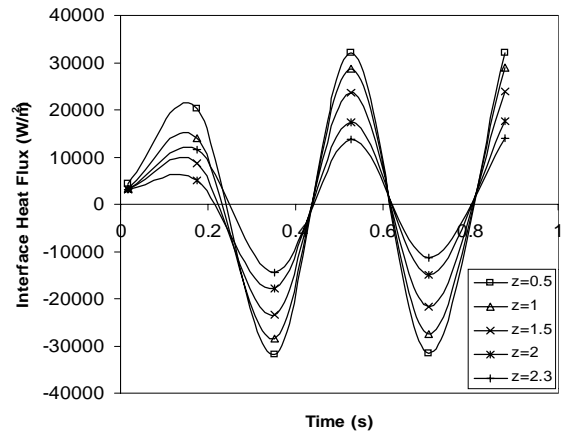

Figure 29: Variation of interface heat flux with time at different sections in the rectangular channel (Re=1600, Bc=0.05 cm, Hc=0.1 cm, g_0= 6.4E8 W/m^3)
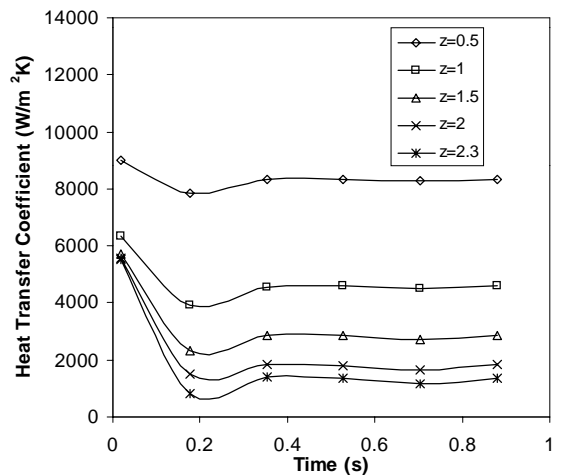

Figure 30: Variation of heat transfer coefficient with time at different sections in the rectangular channel (Re=1600, Bc=0.05 cm, Hc=0.1 cm, g_0= 6.4E8 W/m^3)

Figure 29 shows the variation of interfacial heat flux in the channel with time at different sections of the channel for Re=1600 and dimensions of 0.05*0.1cm. Interface heat flux also shows a sinusoidal behavior and it shows higher values near the entrance of the channel. During the cool down phase, the heat flux near the entrance also becomes lower. This is because of larger transport rate at the leading edge of the thermal boundary layer that develops starting at the entrance section.

Figure 30 shows the variation of heat transfer coefficient with time at different locations along the length of the channel for Re=1600 and dimensions of 0.05*0.1cm. After 0.2 seconds heat transfer coefficient remains almost constant for further heating and cooling cycles. Heat transfer coefficient decreases along the channel length. Fluid gets heated as it passes through the channel. The temperature difference between fluid and solid decreases as one moves along the length of the

channel. Thermal boundary layer grows until fully developed flow is established. Therefore, the heat transfer coefficient is higher at the entrance and decreases downstream. The variation is larger at the
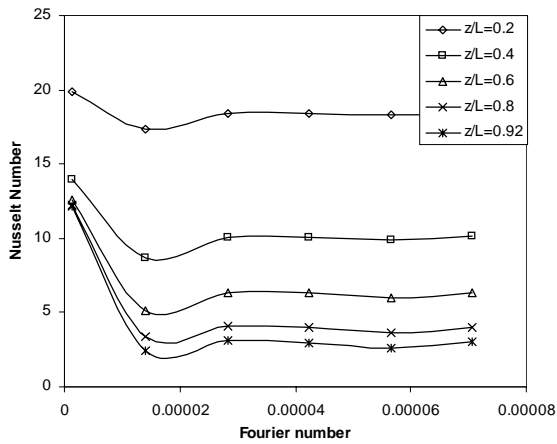

Figure 31: Variation of Nusselt number with time at different sections in the rectangular channel (Re=1600, Bc=0.05 cm, Hc=0.1 cm, g_0= 6.4E8 W/m^3)

entrance because of the rapid development of thermal boundary layer near the leading edge.
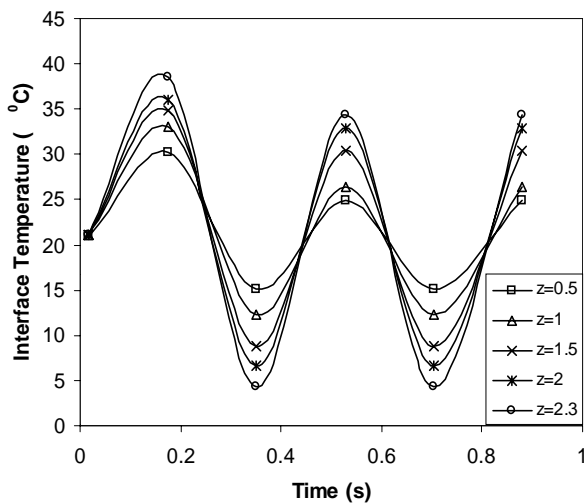

Figure 32: Variation of interface temperature with time at different sections in the rectangular channel with double heat generation rate (g_0= 12.8E8 W/m^3, Re=1600, Bc=0.05 cm, Hc=0.1 cm)

Figure 31 shows variation of Nusselt number with Fourier number at different locations along the length of the channel for Re=1600 and dimensions of 0.05*0.1 cm. The trends are analogous to that seen for the variation of heat transfer coefficient presented in figure 30.

Figures 32 shows the interface temperature variation for heating and cooling cycles. The heat generation rate is 12.8E8 W/m^3 and the channel dimensions are 0.05*0.1 cm. As compared to figure 28, it is seen that the interface temperature variation increases as the heat generation rate is doubled. The increase is seen in all locations within the channel. Figures 33 shows the Nusselt number variation for g_0= 12.8E8 W/m^3 and channel dimensions

of 0.05*0.1 cm. It may be noted that at all locations, the Nusselt number is highest at the beginning of the transient, decreases rapidly with time and undershoots before settling to a constant value for that location.
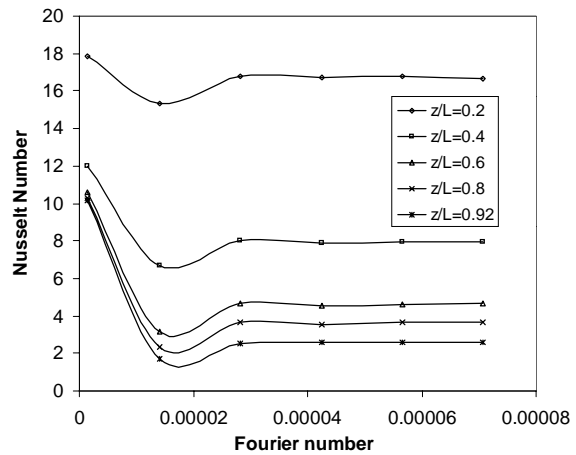

Figure 33: Variation of Nusselt number with time at different sections in the rectangular channel with double heat generation rate (g_0= 12.8E8 W/m^3, Re=1600, Bc=0.05 cm, Hc=0.1 cm)

The undershoot is caused by rapid distribution of heat between solid and fluid as they both store and release thermal energy at different rate until settling for a periodic equilibrium condition.
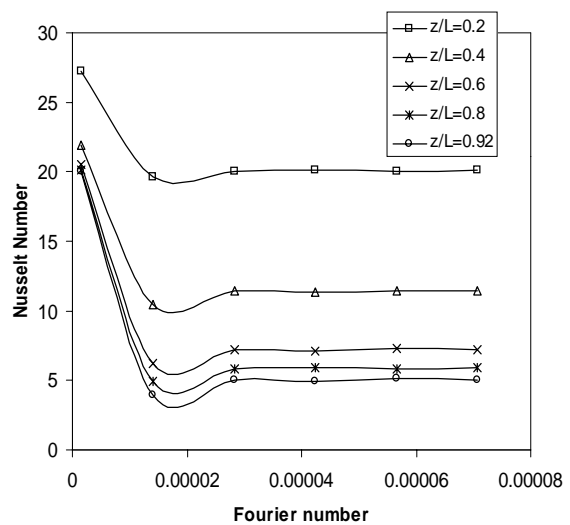

Figure 34: Variation of Nusselt number with time at different sections in a square channel (Re=1600, Bc=0.1 cm, Hc=0.1 cm, g_0= 6.4E8 W/m^3)

Figure 34 shows the variation of Nusselt number with Fourier number at different locations along the length of the channel. Reynolds number of the fluid is 1600 and channel dimensions are 0.1x0.1 cm. As compared to a rectangular channel with dimensions of 0.05*0.1 cm, more amount of fluid is passing through this square channel. Therefore, the values of interface temperature are lower than that of the rectangular channel and consequently the Nusselt number is higher.

CONCLUSIONS

For the steady state analysis with volumetric heat generation in the substrate, it was seen that Nusselt number decreases as one moves along the x or y-axis from the mid-section of the channel to the corner. This is due to smaller fluid velocity caused by larger frictional resistance at the corner. In rectangular channels, heat transfer coefficient values are higher on the longer side than on the shorter side. At a smaller flow rate local Nusselt number decreased and the outlet temperature increased as the low velocity fluid remained in contact with the solid for longer time. Heat transfer coefficient and Nusselt number at a particular cross section in the channel remains almost the same for different heat generation rates. The peripheral average heat transfer coefficient and Nusselt number decreases along the length of the channel due to the development of thermal boundary layer. Large variation in the Nusselt number near the entrance can be attributed to large growth rate of thermal boundary layer near the leading edge. It is seen that the maximum temperature in the channel decreases as the Reynolds number increases. The pressure drop in the channel increases as the Reynolds number increases. Nusselt number increases as the channel dimensions increase. For the same channel, Nusselt number increases with Reynolds number. As the heat generation rate is doubled the interface temperature increases, but there is no significant increase in Nusselt number. For the same amount of heat generation rate and same Reynolds number the corresponding values of interface temperature are lower in a square channel. For the same aspect ratio and same heat generation rate, interface temperature increases as the Reynolds number is decreased. This is because the fluid remains in contact with the solid for a longer period of time. For the transient start-up of heating, it is seen that the interface temperature values increase as one moves along the length of the channel. After a certain period of time, all the parameters reach a steady state, after which there is no further increase in the values of these parameters. For the transient analysis with time dependent heat source, periodic behavior of temperature in the solid as well as in the fluid was seen as the magnetic field was introduced and released. Interface heat flux also showed a periodic behavior and it showed higher values near the entrance of the channel. It is seen that after a certain period of time, local heat transfer coefficient and Nusselt number distribution reach an equilibrium condition and does not change any more with time.

ACKNOWLEDGEMENTS

REFERENCES

[1] Rujano J.R. and Rahman M.M., 1997, "Transient response of Microchannel Heat Sinks in a Silicon Wafer," Journal of Electronic Packaging, 119, pp. 239-246.

[2] Papautsky I., Gale B., Mohanty S., Ameel T. and Frazier B., 1999, "Effects of rectangular microchannel aspect ratio on laminar friction constant," SPIE, 3877, pp. 147-158.

[3] Qu W., Mala G. M. and Lee D., 2000, "Heat transfer for water flow in trapezoidal silicon microchannnels," International Journal of Heat and Mass Transfer, 43(21), pp. 3925-3936.

[4] Chen K. and Wu Y., 2000, "Thermal analysis and simulation of the microchannel flow in miniature thermal conductivity detectors," Sensors and Actuators, 79, pp. 211-218.

[5] Pfund D., Rector D., Shekarriz A., Popescu A. and Welty J., 2000, "Pressure drop measurements in a microchannel," AIChE Journal, 46, pp. 1496-1507.

[6] Rahman M.M., 2000, "Measurements of heat transfer in microchannel heat sinks," International Communications in Heat and Mass Transfer, 27(1), pp. 495-506.

[7] Fedorov A.G. and Viskanta R., 2000, "Three-dimensional conjugate heat transfer in the microchannel heat sink for electronic packaging," International Journal of Heat and Mass Transfer, 43, pp. 399-415.

[8] Wang H, Lovenitti P, Harvey E. and Masood S., 2001, "A simple approach for modeling flow in a microchannel," SPIE, 4236, pp. 99-106.

[9] Lee W.Y, Wong M. and Zohar Y., 2001, "Flow separation in constriction microchannels," IEEE Micro Electro Mechanical Systems (MEMS), pp. 495-498.

[10] Quadir G.A., Mydin A. and Seetharamu K.N., 2001, "Analysis of microchannel heat exchangers using FEM," International Journal of Numerical Methods for Heat and Fluid Flow, 11, pp. 59-75.

[11] Bendib S. and Olivier F., 2001, "Analytical study of microchannel and passive microvalve application to micropump simulator," SPIE, 4593, pp. 283-291.

[12] Zhao H.Y. and Liao W.Y., 2002, "Thermal effects on electro-osmotic pumping of liquids in microchannels," Journal of Micromechanics and Microengineering, 12, pp. 962-970.

[13] Yang C., Beng C. and Chan V., 2002, "Transient analysis of electroosmotic flow in a slit microchannel," Journal of Colloid and Interface Science, 248(2), pp. 524-527.

[14] Jiang L., Wong M. and Johar Y., 2000, "Unsteady characteristics of a thermal microsystem," Sensors and Actuators A: Physical, 82, pp. 108-113.

[15] DeGregoria A.J., Feuling L.J., Laatsch J.F., Rowe J.R., Trueblood J.R. and Wang A.A., 1992, "Test results of an active magnetic regenerative refrigerator," Advances in Cryogenic Engineering, 37, pp. 875-882.

[16] Zimm C., Jastrab A., Sternberg A., Pecharsky V., Gschneidner K., Osborne M. and Anderson I.,

1998, "Description and performance of a near-room temperature magnetic refrigerator," Advances in Cryogenic Engineering, 43, pp. 1759-1766.

[17] Pecharsky V.K. and Gschneidner K.A., 1999, "Magnetocaloric effect and magnetic refrigeration," Journal of Magnetism and Magnetic Materials, 200, pp. 44-56.

[18] Bejan A., 1994, Convection Heat Transfer, 2nd ed., Wiley, New York, N.Y.